Nanoscale

Dynamics of Charge-Transfer Excitons in a Transition Metal Chalcogenide Heterostructure

Journal:	*Nanoscale*
Manuscript ID	NR-ART-03-2020-001924
Article Type:	Paper
Date Submitted by the Author:	07-Mar-2020
Complete List of Authors:	Bian, Ang; Beijing Jiaotong University, Institute of Optoelectronic Technology He, Dawei; Beijing Jiaotong University Hao, Shengcai; Beijing Jiaotong University Fu, Yang; Beijing Jiaotong University Zhang, Lu; Beijing Jiaotong University, He, Jiaqi; Beijing University of Chemical Technology Wang, Yongsheng; Beijing Jiaotong University Zhao, Hui; University of Kansas, Physics and Astronomy

Journal Name

ARTICLE TYPE

Cite this: DOI: 10.1039/xxxxxxxxxx

Dynamics of Charge-Transfer Excitons in a Transition Metal Dichalcogenide Heterostructure

Ang Bian,[a] Dawei He,[a] Shengcai Hao,[a] Yang Fu,[a] Lu Zhang,[a] Jiaqi He,[b] Yongsheng Wang,*[a] and Hui Zhao*[c]

Received Date
Accepted Date

DOI: 10.1039/xxxxxxxxxx

www.rsc.org/journalname

Charge-transfer excitons are formed by photoexcited electrons and holes following charge transfer across a heterojunction. They are important quasiparticles for optoelectronic applications of semiconducting heterostructures. The newly developed two-dimensional heterostructures provide a new platform to study these excitons. We report spatially and temporally resolved transient absorption measurements on the dynamics of charge-transfer excitons in a $MoS_2/WS_2/MoSe_2$ trilayer heterostructure. We observed a non-classical lateral diffusion process of the charge-transfer excitons with a decreasing diffusion coefficient. This feature suggests that hot charge-transfer excitons with large kinetic energies are formed and their cooling process persists for about 100 ps. The long energy relaxation time of excitons in the trilayer compared to its monolayer components is attributed to the reduced carrier and phonon scattering due to the dielectric screening effect in the trilayer. Our results help develop in-depth understanding of the dynamics of charge-transfer excitons in two-dimensional heterostructrues.

1 Introduction

Since 2004, two-dimensional (2D) materials, such as graphene, transition metal dichalcogenides (TMDs), transition metal oxides, hexagonal boron nitride, and phosphorene, have drawn considerable interests[1–4]. Due to the nanoscale thickness, they possess many features that are attractive to both fundamental research and applications as individual materials[5–11]. However, one of the most promising aspects of these 2D materials is the possibility of fabricating heterostructures by combining two or more of them[12]. Since lattice match is no longer a limiting factor thanks to the van der Waals interlayer coupling, a large number of materials can be chosen from to assemble multilayers with certain desired properties. For example, combining graphene with TMDs is beneficial for optoelectronic devices since they have excellent transport and optical properties, respectively, while Morié superlattices formed in TMD-TMD heterostructures can achieve lateral modulation of the electronic properties[13–16].

The 2D heterostructures provide a new and well-controlled platform to study charge-transfer excitons, which play key roles in many optoelectronic devices based on heterostructures. In a semiconductor, photoexcitation results in pairs of electrons and holes. Due to their Coulomb attraction, an electron and a hole can form a bound state known as the exciton. In a heterostructure, one of the charge carriers in an electron-hole pair excited in one material can transfer to the other side of the junction, if the energy configuration favors so. The transferred charge carrier can still form an exciton with the residing carrier. Such charge-transfer excitons have been extensively studied in organic semiconductors as the dominant mechanism of photoexcitation and photocarrier dynamics[17–20]. In 2D heterostructures, such excitons are also called interlayer excitons since the electrons and holes reside in different layers.

Study of charge-transfer excitons in 2D heterostructures has gain significant momentum in recent years owing to their importance in optoelectronic applications based on such materials. Existence of charge-transfer excitons in 2D heterostructures has been demonstrated in time-resolved[21–23] and spectroscopic[24,25] measurements. Because of the separation of electrons and holes in both the real and the momentum space, the charge-transfer excitons have shown long lifetimes[26–28] and novel spin/valley properties[29–33]. Effective control of charge-transfer excitons by electric field has been achieved[32,34,35] and various optoelectronic devices based on them have been demonstrated[36,37].

In contrast to these progress, the dynamics of the charge-transfer excitons in 2D heterostructrues has been less studied. For instance, the time scales of their formation and energy relaxation as well as their lateral transport are still yet to be fully

[a] *Key Laboratory of Luminescence and Optical Information, Ministry of Education, Institute of Optoelectronic Technology, Beijing Jiaotong University, Beijing 100044, China. E-mail: yshwang@bjtu.edu.cn*
[b] *College of Mathematics and Physics, Beijing University of Chemical Technology, Beijing 100029, China*
[c] *Department of Physics and Astronomy, The University of Kansas, Lawrence, Kansas 66045, USA. E-mail: huizhao@ku.edu*

understood. Here we report spatially and temporally resolved measurements to reveal the dynamics of the charge-transfer excitons in a $MoS_2/WS_2/MoSe_2$ trilayer heterostructure. We observed a non-classical lateral diffusion process of these excitons with a decreasing diffusion coefficient. This feature suggests that the energy relaxation of hot charge-transfer excitons occurs on a 100-ps time scale. The significantly slower energy relaxation compared to TMD monolayers is attributed to the reduced carrier and phonon scattering due to the dielectric screening effect in the trilayer. Our study provides experimental information for understanding the dynamics of the charge-transfer excitons in 2D heterostructrues.

2 Results and Discussion

2.1 Sample design and fabrication

Figure 1 illustrates schematically the structure of the heterostructure and the dynamics of the charge-transfer excitons to be studied. The sample is composed of monolayers of $MoSe_2$, WS_2, and MoS_2. According to first-principles calculations[38,39], this trilayer heterostructure has ladder band alignments in both the conduction and the valence bands, as illustrated in the inset of Figure 1. After photoexcitation of some or all of these layers, electrons and holes rapidly populate the MoS_2 and $MoSe_2$ layers, respectively, where their lowest energy states reside. After such charge-transfer processes, the electrons in MoS_2 and the holes in $MoSe_2$ form charge-transfer excitons, which dynamics is studied by measuring transient absorption of a probe pulse.

The optical microscope image of $MoS_2/WS_2/MoSe_2$ trilayer sample is shown in Figure 2(a). The sample was fabricated by mechanical exfoliation and dry transfer techniques[40]. The monolayer flakes of MoS_2, WS_2, and $MoSe_2$ were exfoliated from their bulk crystals (acquired from 2D Semiconductors) by adhensive tapes to polydimethylsiloxane (PDMS) substrates. Their monolayer thickness was identified according to their optical contrasts on PDMS[40] and further confirmed by their photoluminescence (PL) yields. A Si substrate with a 270-nm SiO_2 cap layer was

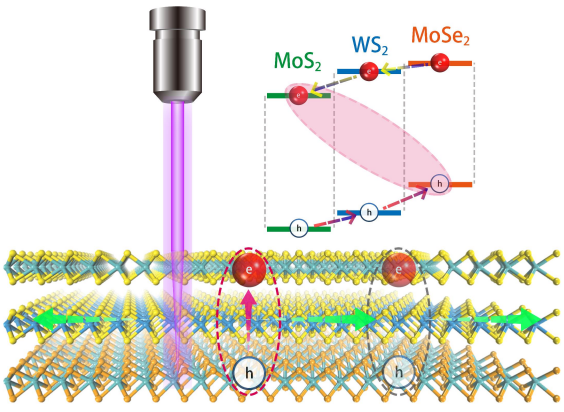

Fig. 1 Schematics of the charge-transfer exciton dynamics studied. A laser pulse excites electron-hole pairs in all three layers of the trilayer sample. Due to the band alignment shown in the inset, electrons and holes transfer to the MoS_2 and $MoSe_2$ layers, respectively. Charge-transfer excitons are formed and then diffuse laterally in the sample.

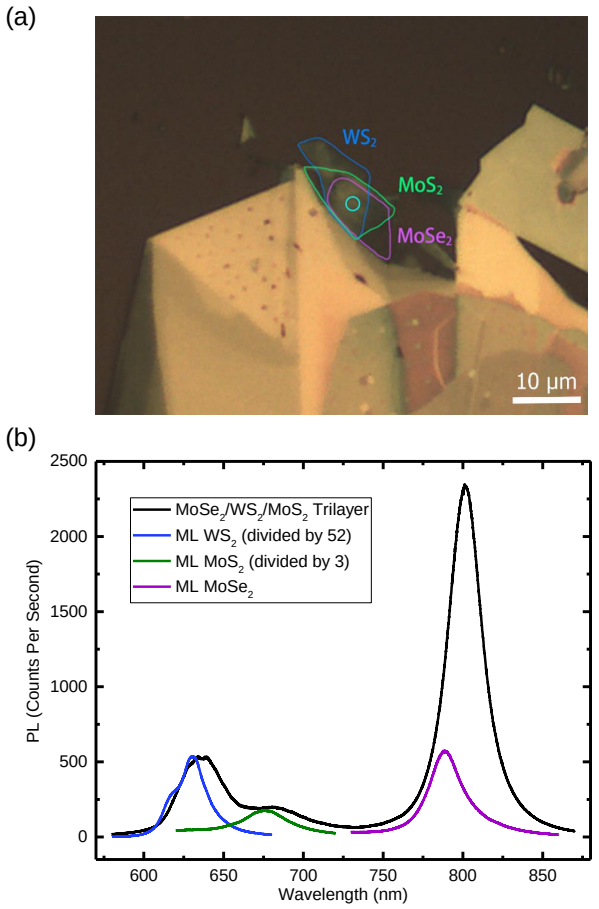

Fig. 2 (a) An optical microscope image of the $MoS_2/WS_2/MoSe_2$ sample studied. (b) Photoluminescence spectra of the heterostructure and the three individual monolayer samples.

cleaned by being soaked in acetone in an ultrasonic bath. The $MoSe_2$ monolayer was first transferred from the PDMS to the Si substrate by pushing it against the substrate and then slowly peeling off, performed under a long-working-distance microscope. Next, the WS_2 monolayer was transferred on top of $MoSe_2$ using the same method. Finally, the MoS_2 monolayer was transferred. After each transfer, the samples was annealed at 200°C in a H_2/Ar environment with a base pressure of about 5 Torr for 2 hours. These annealing steps are crucial to produce high quality interfaces between the monolayers.

2.2 Photoluminescence

We first performed steady-state PL spectroscopy of the trilayer as well as the three monolayer samples at room temperature. Figure 2(b) shows the PL spectra obtained under the excitation of a 532-nm continuous-wave laser beam with an incident power of 0.4 mW. The blue, green, and purple curves represent the spectra from WS_2, $MoS2_2$, and $MoSe_2$ monolayers, respectively, while the black curve is that from the trilayer heterostructure. The WS_2 excitonic peak in the trilayer is quenched by about 52 times compared to the individual WS_2 monolayer. As the middle layer of the trilayer heterostructure, electrons and holes excited in WS_2

can quickly transfer to MoS_2 and $MoSe_2$, respectively, instead of radiatively recombine in WS_2. Energy transfer to the other two layers could also contribute to the PL quenching[41]. The large quenching factor indicates efficient transfer and thus good interface quality. The MoS_2 peak is quenched by a factor of 3. The relatively less pronounced PL quenching of MoS_2 in heterostructures have been generally observed[21,42] and could be due to the relatively low PL yield of MoS_2. Finally, the peak corresponding to the excitonic resonance of $MoSe_2$ is increased by about a factor of 4. This could be attributed to the effect of hole transfer from the other two layers that could compensates for the loss of electrons to the other layers, since $MoSe_2$ is n-doped[43] or gain of carriers by energy transfer from the other layers.

2.3 Transient absorption measurements

The dynamics of the charge-transfer excitons in the $MoS_2/WS_2/MoSe_2$ heterostructure was studied by transient absorption microscopy in reflection geometry[44]. A Ti-doped sapphire laser produces 820-nm and 100 fs pulses with a repetition rate of 80 MHz. One part of this output was focused to a barium borate crystal (BBO) crystal to generate its second harmonic at 410 nm, serving as the pump pulse. The rest of the 820-nm output pumps an optical parametric oscillator (OPO), which signal output in the visible range was used as the probe. The pump and probe beams are combined by a beamsplitter and are sent to a microscope objective lens. The reflected probe is measured by a silicon photodiode with a lock-in amplifier. A mechanical chopper is used to modulate the pump intensity at 2 kHz for the lock-in detection. With this setup, we measured the differential reflection of the probe, which is defined as $\Delta R/R_0 = (R - R_0)/R_0$, where R and R_0 are the probe reflection with and without the presence of the pump beam, respectively. This quantity monitors the density of the photocarriers in the sample[44,45]. It can be measured as a function of space by tilting a mirror in the pump arm with a motorized mirror mount, and thus scanning the probe laser spot at the sample. For a certain probe location, the differential reflection can be measured as a function of the probe delay by changing the length of the probe arm by a linear stage. The time resolution of this setup is about 250 fs, which is limited by the pulse width at the sample location. This is sufficient for the study of exciton dynamics on a 200 ps time range (to be discussed below). All the measurements were performed with the sample at room temperature and under ambient condition.

The 410-nm pump pulse, focused to a spot size of about 1.8 μm in full width at half maximum, injects photocarriers in all three layers of the heterostructure sample. Due to the band alignment shown in Figure 1(a), the excited electrons and holes transfer to the MoS_2 and $MoSe_2$ layers, respectively, followed by formation of charge-transfer excitons. In our study, we monitor the charge-transfer excitons by a probe tuned to the excitonic resonance of the MoS_2 layer. The probe spot size is about 2 μm. To find the best probe wavelength, the peak differential reflection signal was measured as a function of the probe wavelength, with a pump fluence of 2.2 μJ cm^{-2}. The peak value of the differential reflection was obtained by scanning the probe delay near the zero delay (defined when the peaks of the pump and probe pulses overlap in time) to find the maximum signal. As shown in Figure 3(a), the spectrum of the differential reflection signal is consistent with the MoS_2 excitonic resonance of the trilayer, which is shown in Figure 2(b). This confirms that the probe indeed senses the charge-transfer excitons through transient absorption associated with this resonance.

We next measured the peak differential reflection signal as a function of the injected carrier density, with a probe wavelength of 683 nm. The result is shown in Figure 3(b). Here, the injected carrier density is estimated from the pump fluence, assuming that every pump photon absorbed generates one pair of photocarriers. In this process, we used the previously reported absorption coefficients for these three monolayer materials at the pump wavelength[46]. The power dependence shows a clear saturation effect, which has been generally observed in TMD monolayers[47–49]. The data can be satisfactorily fit by a saturable absorption model, $\Delta R/R_0 \propto N/(N+N_s)$, as shown by the solid curve, with a saturation density of $N_s = 2.2 \times 10^{11}$ cm^{-2}.

The temporal dynamics of the charge-transfer excitons is studied by measuring the differential reflection signal as a function of the probe delay. The symbols in Figure 3(c) show the results measured with different values of the pump fluence. The inset of Figure 3(c) shows that at each pump fluence, the signal reaches a peak on an ultrafast time scale that is limited by the pulse width, and is followed by a fast decrease to about 80 % of the peak value. Considering that the pump excites all three layers and the probe mainly senses carriers in MoS_2, these initial fast features could be attributed to the interplay of several carrier processes including excitation of the carriers in MoS_2, transfer of the electrons from the other two layers to MoS_2, transfer of the holes away from MoS_2, interlayer energy transfer, and formation of charge-transfer excitons. Given that these processes all occur on ultrafast time scales, isolation of them from each other is difficult. After these transient processes, the slower decay of the signal can be well fit by a single-exponential function, as shown by the curves in Figure 3(c). The deduced decay time constants are plotted in Figure 3(d). We attribute the decay of the signal to the recombination of the charge-transfer excitons. The slight decrease of the charge-transfer exciton lifetime with density can be attributed to exciton-exciton annihilation, which has been generally observed in TMD monolayers[45,50,51]. We note that with a density-dependent time constant, the decay is nonexponential, strictly speaking. Indeed, the exponential fits for high-density data are not as well as those of low densities, as can be seen in Figure 3(c). Nevertheless, at low densities the decay time is still well defined and accurately reflects the density-independent exciton dynamics.

The above interpretation of the transient absorption data based on charge-transfer excitons illustrated in Figure 1 is reasonable, despite the lack of direct spectroscopic evidence of the formation of charge-transfer excitons. First of all, it has been shown that in heterostructures with ladder band alignments, electrons and holes populated the two outmost layers where their respective band extremes are located, following the ultrafast interlayer charge transfer[40,52]. Second, the charge-transfer exci-

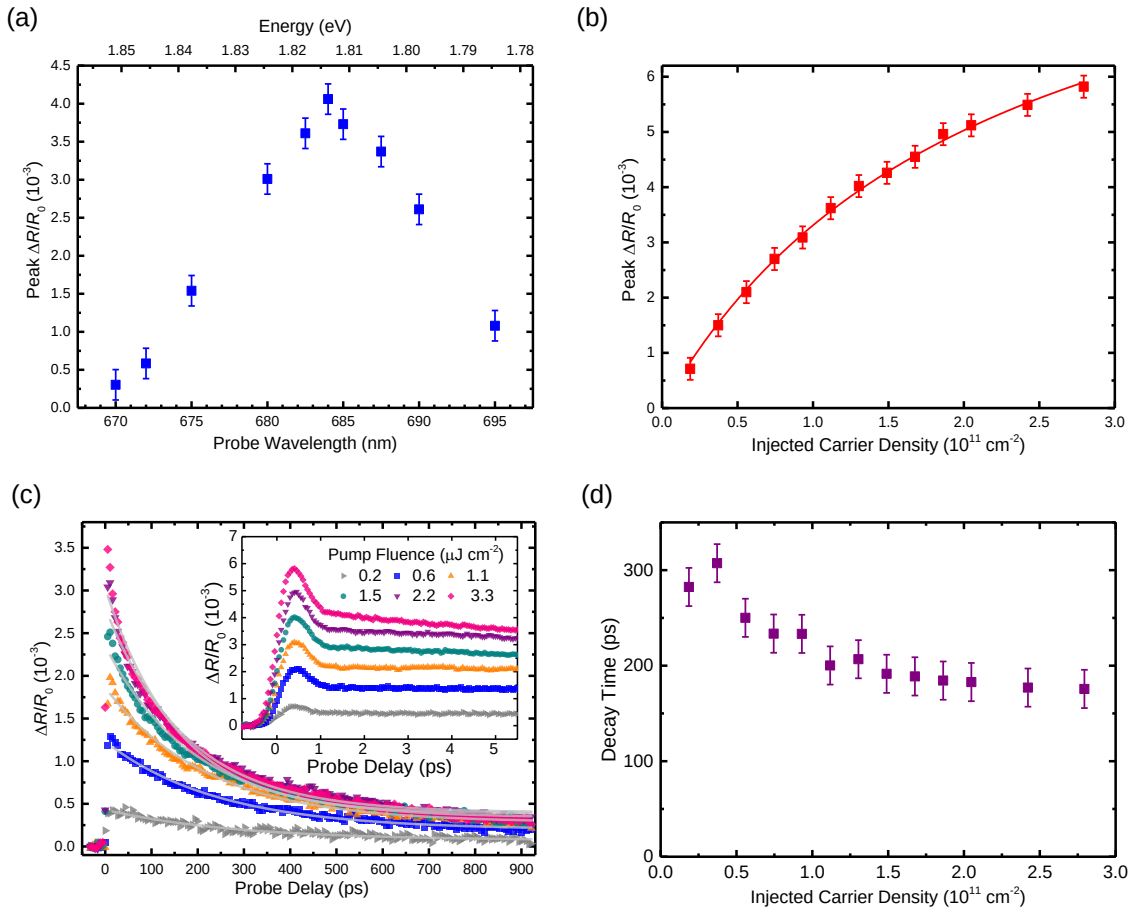

Fig. 3 (a) Peak differential reflection signal of the $MoS_2/WS_2/MoSe_2$ heterostructure as a function of the probe wavelength. (b) Peak differential reflection signal as a function of the injected carrier density by the pump pulse. The solid curve is a fit (see text). (c) Differential reflection signal as a function of the probe delay. The inset shows the signal at early probe delays. (d) The decay time constant of the signal as a function of the injected carrier density, deduced from single-exponential fits to the data. Error bars reflect the uncertainties in the fit.

tons in the trilayer should be stable at room temperature due to their expected large binding energy: Charge-transfer excitons have been generally observed in bilayer heterostructures with a type-II band alignment, such as MoS_2/WSe_2 [24], MoS_2/WS_2 [53], $MoSe_2/WSe_2$ [14,26,53], and WS_2/WSe_2 [16], with binding energies on the order of several hundred meV. Several theoretically works have shown that even if the two carrier-populated layers are separated by several layers of boron nitride, the binding energy is only reduced by less than half[54,55], which is still much larger than the thermal energy at room temperature of 26 meV. Indeed, charge-transfer excitons have been observed at room temperature in two MoS_2 layers separated by two boron nitride layers[56]. Third, ultrafast exciton formation in such trilayer heterostructures can be reasonably assumed based on results from heterobilayers. The ultrashort formation time of hot charge-transfer excitons on the order of 50 fs has been determined experimentally in a MoS_2/WS_2 heterobilayer[57]. Theory has also indicated ultrafast formation of charge-transfer excitons in heterobilayers[58]. In summary, it is thus reasonable to assume that the 200-ps dynamics observed in dominated by charge-transfer excitons.

2.4 Spatially resolved transient absorption measurements

To study the lateral transport properties of the charge-transfer excitons, we performed spatiotemporally resolved differential reflection experiments. Such measurements were achieved by measuring the differential reflection signal as a function of the probe delay as the probe position was scanned. Figure 4(a) is a contour map of the differential reflection signal. As can be seen, the signal at each probe delay has a Gaussian-like spatial profile, which decays with the probe delay. Figure 4(b) shows a few examples of the spatial profiles of the differential reflection signal, with probe delays of 3 (black squares), 12 (red circles), 53 (blue triangles), and 211 ps (purple diamonds), respectively. As indicated by the solid curves, all the profiles can be fit well with Gaussian functions. From the fits to all the measured profiles, we deduce the width of the profiles, w, measured in full width at half maximum. The squared width, w^2, is plotted in Figure 4(c) as a function of the probe delay.

The spatiotemporal evolution of the differential reflection signal monitors the dynamics of the charge-transfer excitons after the photoexcitation. If the charge-transfer excitons undergo a classical diffusion process, their density, N, is expected to follow

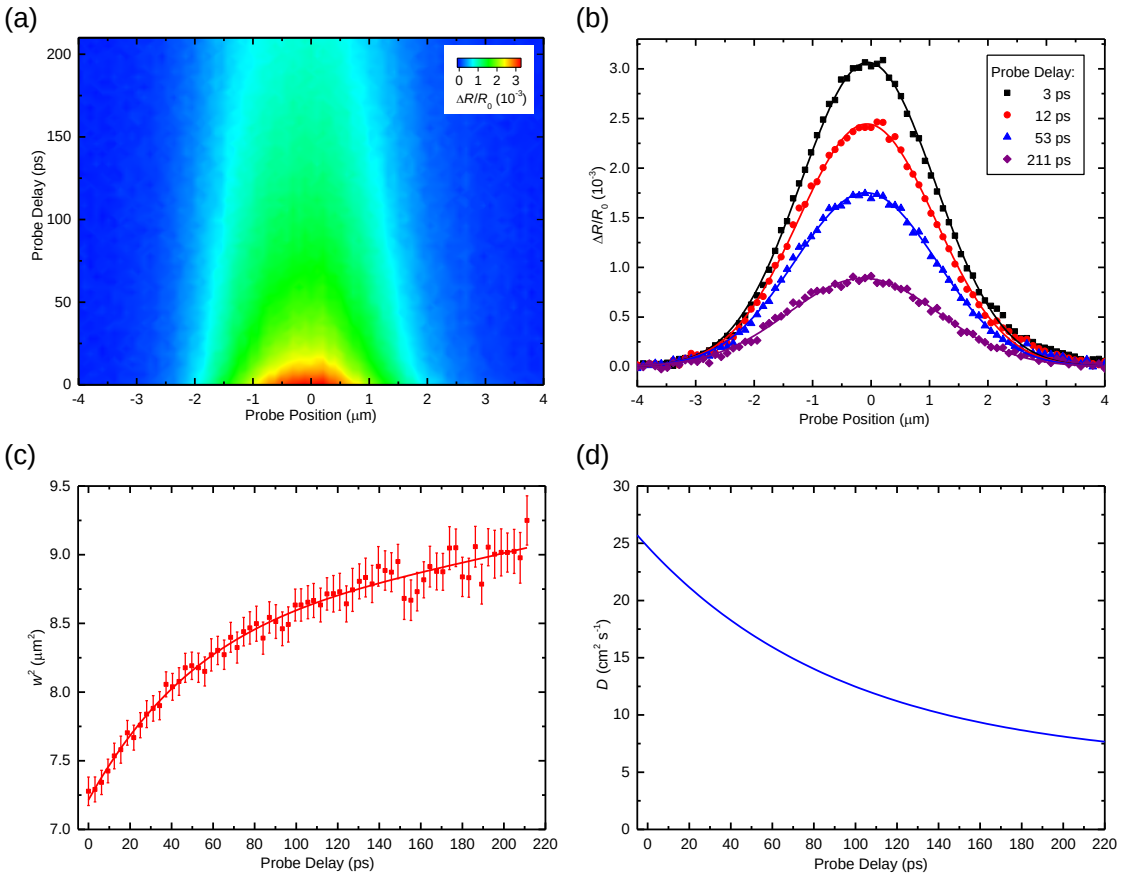

Fig. 4 (a) The differential reflection signal of the $MoS_2/WS_2/MoSe_2$ heterostructure as a function of probe position and probe delay. (b) A few examples of the differential reflection profile at different probe delays. The solid curves are Gaussian fits. (c) Squared width of the profile as a function of the probe delay. The solid curve is a fit by the model discussed in the text. The error bars are obtained from the uncertainties in the Gaussian fits. (d) Time-dependent diffusion coefficient deduced from the fit shown in (c).

the diffusion-recombination equation[59],

$$\frac{\partial N(r,t)}{\partial t} = D\nabla^2 N(r,t) - \frac{N(r,t)}{\tau}, \quad (1)$$

where D and τ are the exciton diffusion coefficient and lifetime, respectively. With an initial Gaussian profile with a width of w_0 and a height of N_0, the solution reads

$$N(r,t) = \frac{w_0^2 N_0}{w^2(t)} \exp[\frac{-t}{\tau}] \exp[-4\ln(2)\frac{r^2}{w^2(t)}], \quad (2)$$

where

$$w^2(t) = w_0^2 + 16\ln(2)Dt. \quad (3)$$

Hence, the squared width is expected to increase linearly with time, with the slope related to the diffusion coefficient. Previously, it has been shown that the exciton transport in individual semiconducting monolayers follows this classical diffusion model well[60–68]. However, the feature shown in Figure 4 distinctly deviates from this model. The profile expansion is sub-linear with a decreasing slope, which suggests that the diffusion coefficient decreases with time.

Since the diffusion is activated by thermal motion of the excitons, the diffusion coefficient is related to the exciton temperature, T. Indeed, the diffusion coefficient and the charge mobility (μ) is related by the Einstein's relation,

$$D = k_B T \mu / e, \quad (4)$$

where k_B and e are the Boltzmann constant and the elementary charge, respectively. Assuming that the mobility is independent of the exciton temperature, the diffusion coefficient is proportional to the temperature. This assumption is reasonable since the exciton-exciton scattering does not cause loss of momentum of the whole exciton assemble. Hence, the decrease of the diffusion coefficient with time could be attributed to the cooling (or energy relaxation) of the hot excitons. Since in the energy relaxation process the exciton temperature decreases exponentially, we can write the time-dependent diffusion coefficient as

$$D(t) = D_0 \exp(-t/\tau_R) + D_{RT}, \quad (5)$$

where D_{RT} represents the diffusion coefficient when the exciton temperature reaches the lattice temperature (which is at room temperature) and τ_R is the energy relaxation time. As an approximation, we consider the energy relaxation as a slow process compared to diffusion so that the solution of the diffusion equation still holds, but with a time-dependent diffusion coefficient.

In this case, eq. 3 becomes

$$w^2(t) = w_0^2 + 16\ln(2)[D_0\exp(-t/\tau_R) + D_{RT}]t. \quad (6)$$

This equation was used to fit the data and the results are satisfactory, as shown by the solid curve in Figure 4(c). The fit parameters are $w_0^2 = 7.2\ \mu m^2$, $D_0 = 19\ cm^2\ s^{-1}$, $D_{RT} = 5.7\ cm^2\ s^{-1}$, and $\tau_R = 97$ ps. These values indicate that the diffusion coefficient drops from the initial value of $D_0 + D_{RT} = 24.7\ cm^2\ s^{-1}$ to $5.7\ cm^2\ s^{-1}$ with a time constant of 97 ps, as the result of the cooling of the charge-transfer excitons. The time evolution of the diffusion coefficient deduce from this fit is plotted in Figure 4(d).

The observation of the time-dependence exciton diffusion coefficient appears to suggest the following picture for the dynamics of charge-transfer excitons: Upon injection of the electron-hole pairs in each of the three monolayers, electrons and holes transfer to the MoS_2 and $MoSe_2$ layers, respectively, on an ultrafast time scale. These carriers possess rather large kinetic energies in their respective layers. Consequently, they form hot charge-transfer excitons with large kinetic energies. Here, the hot excitons refer to those with the electron and hole occupy the MoS_2 and $MoSe_2$ layers, respectively, and with large kinetic energy and in-plane momentum. These hot excitons relax their kinetic energy on a time scale of about 100 ps. During this process, their diffusion coefficient decrease toward the thermalized value of about 5.7 $cm^2\ s^{-1}$.

It should be noted that, due to the finite size of the probe spot, the profiles measured are the convolutions of the actual exciton density profiles and the intensity profile of the probe spot. However, since both profiles are Gaussian functions, their convolution is still a Gaussian function with a squared width equals to the sum of the squared widths of the two profiles. As such, this convolution effect merely adds a constant (squared with of the probe intensity profile) to both sides of Eq. 6, and has no impact on the above analysis.

The dynamics outline above is quite different from *intralayer* excitons in TMD monolayers. It has been shown that the thermalization and energy relaxation in such monolayers occur on a sub-100-fs time scales[69] due to the enhanced carrier-carrier scattering and carrier-phonon scattering caused by the reduced dielectric screening. Since the exciton formation time is about one-order-of-magnitude longer[70] than the cooling time, it is expected that hot carriers relax their excess energy before the formation of cold excitons. However, in the trilayer heterostructure studied here, the dielectric screening is partially recovered, which is expected to suppress the carrier and phonon scattering. As such, it is reasonable to expect a longer energy relaxation time, which is in favor of hot exciton formation. We note that the observed sub-linear profile expansion is similar to previously studied semiconductor quantum wells, where hot exciton relaxation can last hundreds of picoseconds[71,72].

3 Conclusion

In summary, we have observed a non-classical diffusion process of the charge-transfer excitons in a TMD hetero-trilayer of $MoS_2/WS_2/MoSe_2$ by spatially and temporally resolved transient absorption measurements. The diffusion coefficient of the excitons was found to decrease with time during the lifetime of these excitons. A model based on hot exciton cooling was developed, which can describe the dynamics well. These results suggest that hot charge-transfer excitons with large kinetic energies are formed in the heterostructure and their energy relaxation time is about 100 ps, much longer than those in monolayer TMDs. This difference could be attributed to the reduced carrier-carrier and carrier-phonon scattering due to dielectric screening in the trilayer. The extended energy relaxation process could provide opportunities to utilize hot-exciton effect to improve the response time or efficiency of optoelectronic devices[73]. These results are useful for understanding dynamics of charge-transfer excitons in 2D heterostructrues.

Acknowledgements

We are grateful for the financial support of National Key R&D Program of China (2016 YFA0202302), National Natural Science Foundation of China (61527817, 61875236, 61905010, 61975007), Beijing Natural Science Foundation (Z190006), and U.S. National Science Foundation (DMR-1505852).

References

1 K. S. Novoselov, A. K. Geim, S. V. Morozov, D. Jiang, Y. Zhang, S. V. Dubonos, I. V. Grigorieva and A. A. Firsov, *Science*, 2004, **306**, 666–669.

2 K. S. Kim, Y. Zhao, H. Jang, S. Y. Lee, J. M. Kim, K. S. Kim, J. H. Ahn, P. Kim, J. Y. Choi and B. H. Hong, *Nature*, 2009, **457**, 706.

3 Q. H. Wang, K. Kalantar-Zadeh, A. Kis, J. N. Coleman and M. S. Strano, *Nat. Nanotechnol.*, 2012, **7**, 699–712.

4 Z. Lin, A. McCreary, N. Briggs, S. Subramanian, K. H. Zhang, Y. F. Sun, X. F. Li, N. J. Borys, H. T. Yuan, S. K. Fullerton-Shirey, A. Chernikov, H. Zhao, S. McDonnell, A. M. Lindenberg, K. Xiao, B. J. LeRoy, M. Drndic, J. C. M. Hwang, J. Park, M. Chhowalla, R. E. Schaak, A. Javey, M. C. Hersam, J. Robinson and M. Terrones, *2D Mater.*, 2016, **3**, 042001.

5 A. Splendiani, L. Sun, Y. Zhang, T. Li, J. Kim, C. Y. Chim, G. Galli and F. Wang, *Nano Lett.*, 2010, **10**, 1271–1275.

6 K. F. Mak, C. Lee, J. Hone, J. Shan and T. F. Heinz, *Phys. Rev. Lett.*, 2010, **105**, 136805.

7 N. Kumar, S. Najmaei, Q. Cui, F. Ceballos, P. M. Ajayan, J. Lou and H. Zhao, *Phys. Rev. B*, 2013, **87**, 161403.

8 Y. Li, Y. Rao, K. F. Mak, Y. You, S. Wang, C. R. Dean and T. F. Heinz, *Nano Lett.*, 2013, **13**, 3329–3333.

9 D. Xiao, G. B. Liu, W. Feng, X. Xu and W. Yao, *Phys. Rev. Lett.*, 2012, **108**, 196802.

10 A. Chernikov, T. C. Berkelbach, H. M. Hill, A. Rigosi, Y. L. Li, O. B. Aslan, D. R. Reichman, M. S. Hybertsen and T. F. Heinz, *Phys. Rev. Lett.*, 2014, **113**, 076802.

11 L. Britnell, R. M. Ribeiro, A. Eckmann, R. Jalil, B. D. Belle, A. Mishchenko, Y.-J. Kim, R. V. Gorbachev, T. Georgiou, S. V. Morozov, A. N. Grigorenko, A. K. Geim, C. Casiraghi, A. H. C. Neto and K. S. Novoselov, *Science*, 2013, **340**, 1311–1314.

12 A. K. Geim and I. V. Grigorieva, *Nature*, 2013, **499**, 419–425.

13 E. M. Alexeev, D. A. Ruiz-Tijerina, M. Danovich, M. J. Hamer, D. J. Terry, P. K. Nayak, S. Ahn, S. Pak, J. Lee, J. I. Sohn, M. R. Molas, M. Koperski, K. Watanabe, T. Taniguchi, K. S. Novoselov, R. V. Gorbachev, H. S. Shin, V. I. Fal'ko and A. I. Tartakovskii, *Nature*, 2019, **567**, 81.

14 K. L. Seyler, P. Rivera, H. Y. Yu, N. P. Wilson, E. L. Ray, D. G. Mandrus, J. Q. Yan, W. Yao and X. D. Xu, *Nature*, 2019, **567**, 66.

15 K. Tran, G. Moody, F. C. Wu, X. B. Lu, J. Choi, K. Kim, A. Rai, D. A. Sanchez, J. M. Quan, A. Singh, J. Embley, A. Zepeda, M. Campbell, T. Autry, T. Taniguchi, K. Watanabe, N. S. Lu, S. K. Banerjee, K. L. Silverman, S. Kim, E. Tutuc, L. Yang, A. H. MacDonald and X. Q. Li, *Nature*, 2019, **567**, 71.

16 C. H. Jin, E. C. Regan, A. M. Yan, M. I. B. Utama, D. Q. Wang, S. H. Zhao, Y. Qin, S. J. Yang, Z. R. Zheng, S. Y. Shi, K. Watanabe, T. Taniguchi, S. Tongay, A. Zettl and F. Wang, *Nature*, 2019, **567**, 76.

17 J. L. Bredas, D. Beljonne, V. Coropceanu and J. Cornil, *Chem. Rev.*, 2004, **104**, 4971–5003.

18 L. A. A. Pettersson, L. S. Roman and O. Inganas, *J. Appl. Phys.*, 1999, **86**, 487–496.

19 P. Peumans, A. Yakimov and S. R. Forrest, *J. Appl. Phys.*, 2003, **93**, 3693–3723.

20 T. R. Kafle, B. Kattel, P. Yao, P. Zereshki, H. Zhao and W. L. Chan, *J. Am. Chem. Soc.*, 2019, **141**, 11328–11336.

21 F. Ceballos, M. Z. Bellus, H. Y. Chiu and H. Zhao, *ACS Nano*, 2014, **8**, 12717–12724.

22 M. Baranowski, A. Surrente, L. Klopotowski, J. M. Urban, N. Zhang, D. K. Maude, K. Wiwatowski, S. Mackowski, Y. C. Kung, D. Dumcenco, A. Kis and P. Plochocka, *Nano Lett.*, 2017, **17**, 6360–6365.

23 F. Ceballos, M. Z. Bellus, H. Y. Chiu and H. Zhao, *Nanoscale*, 2015, **7**, 17523–17528.

24 M. H. Chiu, M. Y. Li, W. Zhang, W. T. Hsu, W. H. Chang, M. Terrones, H. Terrones and L. J. Li, *ACS Nano*, 2014, **8**, 9649–9656.

25 X. Zhu, N. R. Monahan, Z. Gong, H. Zhu, K. W. Williams and C. A. Nelson, *J. Am. Chem. Soc.*, 2015, **137**, 8313–8320.

26 P. Rivera, J. R. Schaibley, A. M. Jones, J. S. Ross, S. Wu, G. Aivazian, P. Klement, K. Seyler, G. Clark, N. J. Ghimire, J. Yan, D. G. Mandrus, W. Yao and X. Xu, *Nat. Commun.*, 2015, **6**, 6242.

27 B. Miller, A. Steinhoff, B. Pano, J. Klein, F. Jahnke, A. Holleitner and U. Wurstbauer, *Nano Lett.*, 2017, **17**, 5229–5237.

28 J. Kunstmann, F. Mooshammer, P. Nagler, A. Chaves, F. Stein, N. Paradiso, G. Plechinger, C. Strunk, C. Schuller, G. Seifert, D. R. Reichman and T. Korn, *Nat. Phys.*, 2018, **14**, 801–806.

29 P. Rivera, K. L. Seyler, H. Y. Yu, J. R. Schaibley, J. Q. Yan, D. G. Mandrus, W. Yao and X. D. Xu, *Science*, 2016, **351**, 688–691.

30 P. Nagler, M. V. Ballottin, A. A. Mitioglu, F. Mooshammer, N. Paradiso, C. Strunk, R. Huber, A. Chernikov, P. C. M. Christianen, C. Schuller and T. Korn, *Nat. Commun.*, 2017, **8**, 1551.

31 W. T. Hsu, L. S. Lu, P. H. Wu, M. H. Lee, P. J. Chen, P. Y. Wu, Y. C. Chou, H. T. Jeng, L. J. Li, M. W. Chu and W. H. Chang, *Nat. Commun.*, 2018, **9**, 1356.

32 A. Ciarrocchi, D. Unuchek, A. Avsar, K. Watanabe, T. Taniguchi and A. Kis, *Nat. Photo.*, 2019, **13**, 131–136.

33 L. Zhang, R. Gogna, G. W. Burg, J. Horng, E. Paik, Y. H. Chou, K. Kim, E. Tutuc and H. Deng, *Phys. Rev. B*, 2019, **100**, 041402.

34 D. Unuchek, A. Ciarrocchi, A. Avsar, K. Watanabe, T. Taniguchi and A. Kis, *Nature*, 2018, **560**, 340.

35 D. H. Luong, H. S. Lee, G. P. Neupane, S. Roy, G. Ghimire, J. H. Lee, Q. A. Vu and Y. H. Lee, *Adv. Mater.*, 2017, **29**, 1701512.

36 J. S. Ross, P. Rivera, J. Schaibley, E. Lee-Wong, H. Y. Yu, T. Taniguchi, K. Watanabe, J. Q. Yan, D. Mandrus, D. Cobden, W. Yao and X. D. Xu, *Nano Lett.*, 2017, **17**, 638–643.

37 Y. D. Liu, H. L. Fang, A. Rasmita, Y. Zhou, J. T. Li, T. Yu, Q. H. Xiong, N. Zheludev, J. Liu and W. B. Gao, *Sci. Adv.*, 2019, **5**, eaav4506.

38 Y. Z. Guo and J. Robertson, *Appl. Phys. Lett.*, 2016, **108**, 233104.

39 C. Gong, H. J. Zhang, W. H. Wang, L. Colombo, R. M. Wallace and K. J. Cho, *Appl. Phys. Lett.*, 2013, **103**, 053513.

40 F. Ceballos, P. Zereshki and H. Zhao, *Phys. Rev. Mater.*, 2017, **1**, 044001.

41 D. Kozawa, A. Carvalho, I. Verzhbitskiy, F. Giustiniano, Y. Miyauchi, S. Mouri, A. H. C. Neto, K. Matsuda and G. Eda, *Nano Lett.*, 2016, **16**, 4087–4093.

42 J. T. Yuan, S. Najmaei, Z. H. Zhang, J. Zhang, S. D. Lei, P. M. Ajayan, B. I. Yakobson and J. Lou, *ACS Nano*, 2015, **9**, 555–563.

43 X. Wang, Y. Gong, G. Shi, W. L. Chow, K. Keyshar, G. Ye, R. Vajtai, J. Lou, Z. Liu, E. Ringe, B. K. Tay and P. M. Ajayan, *ACS Nano*, 2014, **8**, 5125–5131.

44 F. Ceballos and H. Zhao, *Adv. Funct. Mater.*, 2017, **27**, 1604509.

45 N. Kumar, Q. Cui, F. Ceballos, D. He, Y. Wang and H. Zhao, *Phys. Rev. B*, 2014, **89**, 125427.

46 Y. Li, A. Chernikov, X. Zhang, A. Rigosi, H. M. Hill, A. M. van der Zande, D. A. Chenet, E.-M. Shih, J. Hone and T. F. Heinz, *Phys. Rev. B*, 2014, **90**, 205422.

47 S. Q. Zhao, D. W. He, J. Q. He, X. W. Zhang, L. X. Yi, Y. S. Wang and H. Zhao, *Nanoscale*, 2018, **10**, 9538–9546.

48 B. Liu, Y. Z. Meng, X. Z. Ruan, F. Q. Wang, W. Q. Liu, F. Q. Song, X. F. Wang, J. Wu, L. He, R. Zhang and Y. B. Xu, *Nanoscale*, 2017, **9**, 18546–18551.

49 Y. Li, Q. Liu, Q. Cui, Z. Qi, J. Z. Wu and H. Zhao, *Nanoscale*, 2017, **9**, 19360–19366.

50 D. Sun, Y. Rao, G. A. Reider, G. Chen, Y. You, L. Brezin, A. R. Harutyunyan and T. F. Heinz, *Nano Lett.*, 2014, **14**, 5625–5629.

51 H. Liu, C. Wang, D. M. Liu and J. B. Luo, *Nanoscale*, 2019, **11**, 7913–7920.

52 F. Ceballos, M. G. Ju, S. D. Lane, X. C. Zeng and H. Zhao, *Nano Lett.*, 2017, **17**, 1623–1628.

53 A. F. Rigos, H. M. Hill, Y. L. Li, A. Chernikov and T. F. Heinz, *Nano Lett.*, 2015, **15**, 5033–5038.

54 S. Latini, K. T. Winther, T. Olsen and K. S. Thygesen, *Nano Lett.*, 2017, **17**, 938–945.

55 V. der Donck, M. and F. M. Peeters, *Phys. Rev. B*, 2018, **98**, 115104.

56 E. V. Calman, M. M. Fogler, L. V. Butov, S. Hu, A. Mishchenko and A. K. Geim, *Nat. Commun.*, 2018, **9**, 1895.

57 H. Chen, X. Wen, J. Zhang, T. Wu, Y. Gong, X. Zhang, J. Yuan, C. Yi, J. Lou, P. M. Ajayan, W. Zhuang, G. Zhang and J. Zheng, *Nat. Commun.*, 2016, **7**, 12512.

58 S. Ovesen, S. Brem, C. Linderälv, M. Kuisma, T. Korn, P. Erhart, M. Selig and E. Malic, *Commun. Phys.*, 2019, **2**, 23.

59 L. M. Smith, D. R. Wake, J. P. Wolfe, D. Levi, M. V. Klein, J. Klem, T. Henderson and H. Morkoç, *Phys. Rev. B*, 1988, **38**, 5788–5791.

60 R. Wang, B. A. Ruzicka, N. Kumar, M. Z. Bellus, H.-Y. Chiu and H. Zhao, *Phys. Rev. B*, 2012, **86**, 045406.

61 N. Kumar, Q. Cui, F. Ceballos, D. He, Y. Wang and H. Zhao, *Nanoscale*, 2014, **6**, 4915–4919.

62 Q. Cui, F. Ceballos, N. Kumar and H. Zhao, *ACS Nano*, 2014, **8**, 2970–2976.

63 J. He, D. He, Y. Wang, Q. Cui, F. Ceballos and H. Zhao, *Nanoscale*, 2015, **7**, 9526.

64 J. He, D. He, Y. Wang, Q. Cui, M. Z. Bellus, H.-Y. Chiu and H. Zhao, *ACS Nano*, 2015, **9**, 6436–6442.

65 Q. Cui, J. He, M. Z. Bellus, M. Mirzokarimov, T. Hofmann, H.-Y. Chiu, M. Antonik, D. He, Y. Wang and H. Zhao, *Small*, 2015, **11**, 5565–5571.

66 M. Z. Bellus, Z. B. Yang, J. H. Hao, S. P. Lau and H. Zhao, *2D Mater.*, 2017, **4**, 025063.

67 S. Pan, W. Kong, J. Liu, X. Ge, P. Zereshki, S. Hao, D. He, Y. Wang and H. Zhao, *ACS Appl. Nano Mater.*, 2019, **2**, 459–464.

68 Y. Fu, D. He, J. He, A. Bian, L. Zhang, S. Liu, Y. Wang, and H. Zhao, *Adv. Mater. Interfaces*, 2019, **6**, 190137.

69 Z. Nie, R. Long, L. Sun, C. C. Huang, J. Zhang, Q. Xiong, D. W. Hewak, Z. Shen, O. V. Prezhdo and Z. H. Loh, *ACS Nano*, 2014, **8**, 10931–10940.

70 F. Ceballos, Q. Cui, M. Z. Bellus and H. Zhao, *Nanoscale*, 2016, **8**, 11681–11688.

71 H. Zhao, B. Dal Don, S. Moehl, H. Kalt, K. Ohkawa and D. Hommel, *Phys. Rev. B*, 2003, **67**, 035306.

72 H. Zhao, B. Dal Don, G. Schwartz and H. Kalt, *Phys. Rev. Lett.*, 2005, **94**, 137402.

73 S. S. Lim, D. Giovanni, Q. Zhang, A. Solanki, N. F. Jamaludin, J. W. M. Lim, N. Mathews, S. Mhaisalkar, M. S. Pshenichnikov and T. C. Sum, *Sci. Adv.*, 2019, **5**, eaax3620.

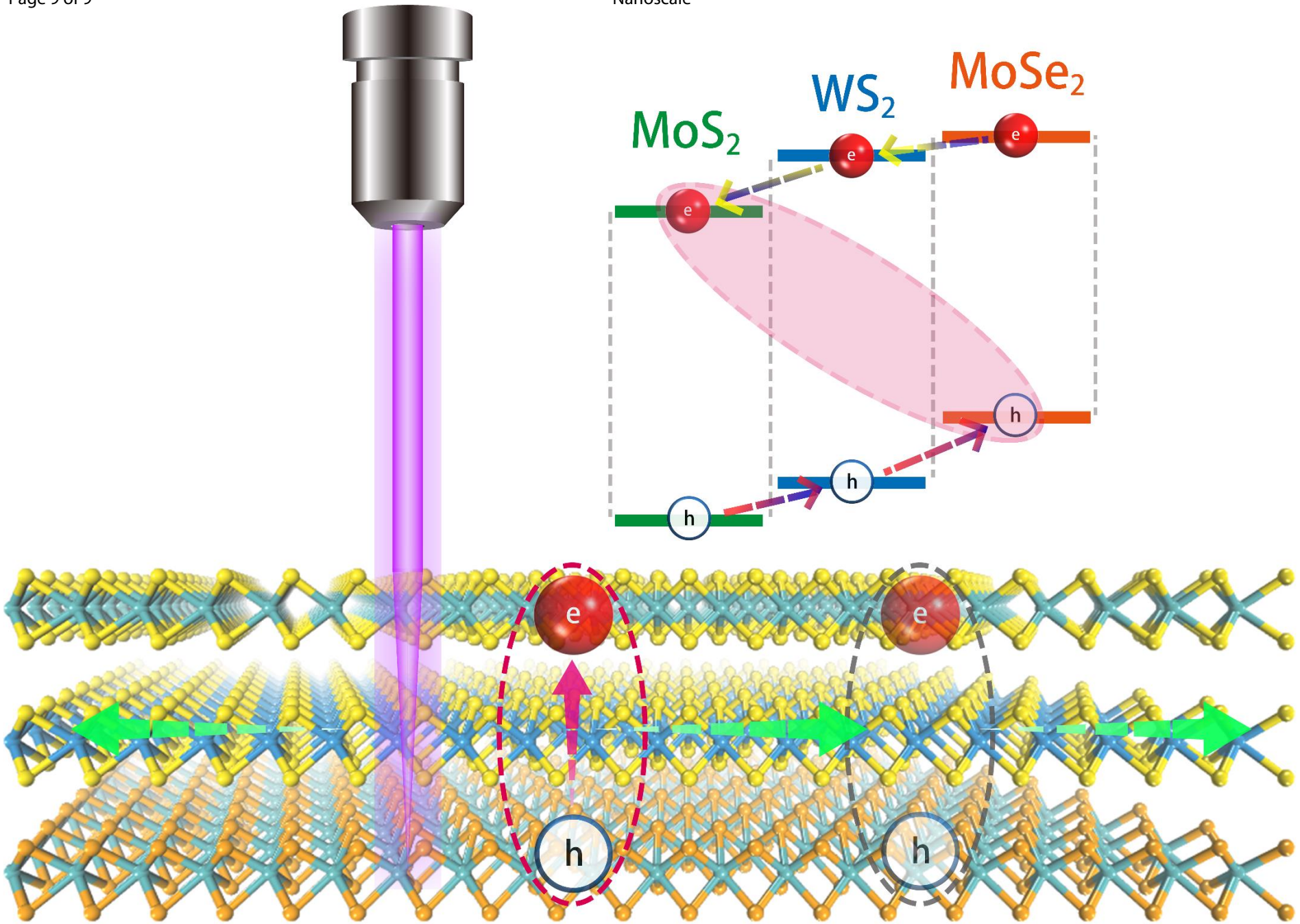
MoS2
WS2
MoSe2
e
e
e
h
h
h
e
e
h
h